AUC-based Resolution in Optical Coherence Tomography

J.P. Rolland[a], J. O'Daniel[a], E. Clarkson[b], K. Cheong[b], A.C. Akcay[a], T. Delemos[a], P. Parrein[a], K.S. Lee[a]

[a]School of Optics/CREOL/FPCE, University of Central Florida, Orlando FL 32816
[b]Optical Science/Radiology Department, University of Arizona, Tucson AZ 85720

ABSTRACT

Optical coherence tomography (OCT) is an interferometric technique using the low coherence property of light to axially image at high resolution in biological tissue samples. Transverse imaging is obtained with two-dimensional scanning and transverse resolution is limited by the size of the scanning beam at the imaging point. The most common metrics used for determining the axial resolution of an OCT system are the full-width-at-half-maximum (FWHM), the absolute square integral (ASI), and the root-mean-square (RMS) width of the axial PSF of the system, where the PSF of an OCT system is defined as the envelope of the interference fringes when the sample has been replaced by a simple mirror. Such metrics do not take into account the types of biological tissue samples being imaged. In this paper we define resolution in terms of the instrument and the biological sample combined by defining a resolution task and computing the associated detectability index and area under the receiver operating characteristic curve (AUC). The detectability index was computed using the Hotelling observer or best linear observer. Results of simulations demonstrate that resolution is best quantified as a probability of resolving two layers, and the impact on resolution of variations in the index of refraction between the layers is clearly demonstrated.

Keywords: Optical coherence imaging, image quality assessment, Hotelling observer, resolution

1. INTRODUCTION

Optical coherence tomography (OCT) is an interferometric technique which is utilized to record temporal or equivalent spatial information carried by the amplitude and phase of the optical fields backscattered or backreflected from a biological sample.[1–3] This technique has found significant application in the area of non-invasive high resolution biomedical imaging across various applications including ophthalmology, dermatology, cardiology, gastroenterology, endoscopic biopsy, and dentistry.[4] Images of fishes eye and mice skin obtained in our laboratory are shown in Fig. 1. OCT operates on the fundamental principle of low-coherence interferometry schematically represented in Fig. 2, where interferences occur only if the optical path difference of fields traveling in the two arms of the interferometer is less than the coherence length of the source. Thus, a short coherence length enables high axial resolution. Examples of light sources employed in OCT are superluminescent diodes and mode-locked Ti:Sapphire lasers. The common properties of these light sources are their radiation in the near-infrared centered at a wavelength between 800 nm and 1550 nm, enabling good penetration of the light into biological samples. Such sources have broad bandwidths from 20 nm up to 150 nm, thus coherence lengths on the order of 1 to 20μm that provide an estimate of axial resolution in OCT. The infrared region of the spectrum allows for deeper penetration inside biological tissues as compared to the visible part of the spectrum.[5] Another important criterion for OCT sources is the emission power which ranges from about 0.1 mW up to about 100 mW.

The axial resolution of an OCT system, defined as half of the source coherence length, may range from as small as 1 μm up to 20 μm with a scanning penetration depth of several millimeters into the sample depending on the source employed and the absorption and scattering characteristics of the sample being imaged. The most common metrics used for determining the resolution of an OCT system are the full-width-at-half-maximum (FWHM), the absolute square integral (ASI), and the root-mean-square (RMS) width of the axial PSF of the system,[6–7] where the PSF of an OCT system is defined as the envelope of the interference fringes when the sample is a mirror. In this paper, we present a theoretical model of OCT imaging which may be used to quantify resolution in terms of the area under the receiver operating characteristic curve (AUC), which bears relation not only to the instrumentation but also to diagnostic imaging.[8] Such approach requires defining a sample model to be imaged and a resolution task. In this investigation, the model sample involves two simple interfaces of slightly

Medical Imaging 2004: Image Perception, Observer Performance, and Technology Assessment, edited by Dev P. Chakraborty, Miguel P. Eckstein, Proceedings of SPIE Vol. 5372 (SPIE, Bellingham, WA, 2004) · 1605-7422/04/$15 · doi: 10.1117/12.535935

different indices of refraction separated by a distance ℓ that will be set to various values in order to study its probability of being resolved. The presence, absence, or strength of specific layers within skin tissue is indicative of healthy or diseased tissue.

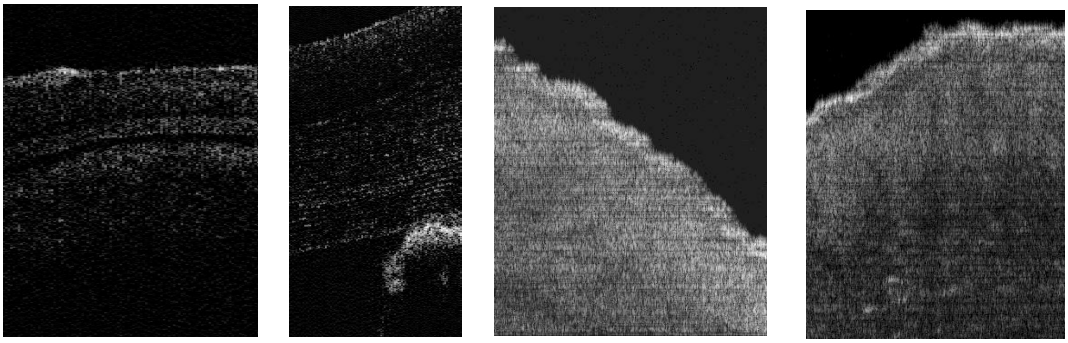

a b c d

Figure 1. OCT images obtained with a 940nm SLD, 70nm bandwidth at 7mW (a-b) Fishes eye; (b-c) Mice skin

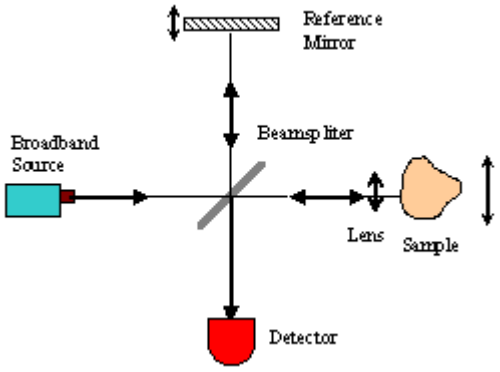

Figure 2. Schematic of a free-space OCT setup

2. METHODS

Let H_0 be the hypothesis under which the interfaces of a layer are superimposed, and let H_1 be the alternative hypothesis where the two interfaces of a layer are separated by a distance ℓ. We shall derive the signal-to-noise ratio (SNR) associated with the Hotelling observer for such task and use this task-based SNR as a measure of the resolving power of the imaging system. This SNR is directly related to the AUC for this observer since the Hotelling observer is linear in the data and, according to the central limit theorem, linear test statistics display Gaussian statistics. The mathematical framework upon which the Hotelling observer is computed fully accounts for the broadband nature of the light source, the vector properties of the propagating field, the geometry of the problem, and the covariance matrix of the detected signals. No assumption is required about the power spectrum of the source. We shall now express the photocurrent in OCT, as well as its mean and covariance, both required to compute the SNR associated with the Hotelling observer.

2.1. Expression of the photocurrent detected in OCT

Given the broadband nature of the light source, let the field emitted by the source be decomposed into its Fourier components as

$$\mathbf{E}_s(t) = \int_{-\infty}^{\infty} \exp(i\omega t)\, \widehat{\mathbf{E}}_s(\omega)\, d\omega \quad , \tag{1}$$

where the symbol hat denotes a function in the Fourier domain. We may express the field at the detector in terms of the field at the source by the expression

$$\begin{aligned}\mathbf{E}(t) &= \int_{-\infty}^{\infty} \alpha_1 \exp\left[i\phi_1(\omega,t) + i\omega t\right] \widehat{\mathbf{E}}_s(\omega)\, d\omega + \\ &\quad \int_{-\infty}^{\infty} \widehat{\beta}_2(\omega) \exp\left[i\phi_2(\omega,t) + i\omega t\right] \widehat{\mathbf{E}}_s(\omega)\, d\omega \quad ,\end{aligned} \tag{2}$$

where the first term represents the field from the reference arm and the second term represents the field from the sample. The term $\alpha_1 \exp\left[i\phi_1(\omega,t) + i\omega t\right]$ contains a real number α_1 that quantifies the relative amplitude at the detector of the wave reflected from the reference mirror, and a phase $\phi_1(\omega,t)$ that accounts for the optical path length to and back from the reference mirror and any phase-induced component from reflection, modulation, dispersion and possibly other effects along the reference arm. The function $\widehat{\beta}_2(\omega)$ is the amplitude at the detector of the component of the wave backscattered from the sample arm at frequency ω and is determined by the refractive index profile of the sample. Finally, the term $\phi_2(\omega,t)$ accounts for the optical path length in air to and from the sample in the sample arm, phase changes due to reflection, dispersion, movement of the sample and possibly other effects. If we write

$$m(\omega,t) = \alpha_1 \exp\left[i\phi_1(\omega,t)\right] + \widehat{\beta}_2(\omega) \exp\left[i\phi_2(\omega,t)\right] \quad , \tag{3}$$

then we have

$$\mathbf{E}(t) = \int_{-\infty}^{\infty} m(\omega,t) \exp(i\omega t)\, \widehat{\mathbf{E}}_s(\omega)\, d\omega \quad . \tag{4}$$

In this expression both $\mathbf{E}(t)$ and $\widehat{\mathbf{E}}_s(\omega)$ are stochastic processes. We assume that the source field $\mathbf{E}_s(t)$ obeys circular Gaussian statistics, thus $\langle \mathbf{E}_s(t) \rangle = 0$. This implies that $\mathbf{E}(t)$ is also a Gaussian random process with $\langle \mathbf{E}(t) \rangle = 0$. The angle brackets $\langle * \rangle$ throughout the paper will be used to indicate statistical averages over all sources of randomness for the quantity inside the bracket. The covariance $\left\langle \mathbf{E}(t)\, \mathbf{E}^{\dagger}(t') \right\rangle$ depends on properties of the source and will be discussed in more detail below.

The detected photocurrent is given by the equation

$$I(t) = \frac{e}{\Delta t} \int_{t-\Delta t}^{t} N(t')\, dt' = \frac{e}{\Delta t} \int_{-\infty}^{\infty} r(t-t')\, N(t')\, dt' \quad , \tag{5}$$

where e is the electron charge, and $r(t)$ denotes the time integration window of the detector and is given by

$$r(t) = \begin{array}{c} 1 \text{ for } 0 \le t \le \Delta t \\ 0 \text{ otherwise} \end{array} \quad . \tag{6}$$

In this integral $N(t)$ is a doubly stochastic Poisson random process representing the photoelectrons produced by the field impinging on the detector. Its conditional mean is given by

$$\overline{N}(t) = \rho \mathbf{E}^{\dagger}(t)\, \mathbf{E}(t) \quad , \tag{7}$$

where ρ is proportional to the detector responsitivity and area. The overall mean of this process may be expressed as

$$\langle N(t) \rangle = \left\langle \overline{N}(t) \right\rangle = \rho \left\langle \mathbf{E}^{\dagger}(t)\, \mathbf{E}(t) \right\rangle \quad . \tag{8}$$

In this equation, $\langle N(t) \rangle$ is the average of $N(t)$ over the Poisson noise associated with detection and the Gaussian noise in the source field. On the other hand, $\left\langle \overline{N}(t) \right\rangle$ averages $\overline{N}(t)$ over the Gaussian statistics only, since the Poisson noise has already been averaged out to get $\overline{N}(t)$.

2.2. Mean value of the photocurrent

The mean value of the photocurrent may be expressed as

$$\langle I(t)\rangle = \frac{e}{\Delta t}\int_{-\infty}^{\infty} r(t-t')\,\langle N(t')\rangle\,dt' \quad , \tag{9}$$

where the expectation in the integrand is given by

$$\rho\int_{-\infty}^{\infty}\int_{-\infty}^{\infty} m^*(\omega,t)\,m(\omega',t)\exp\left[i(\omega'-\omega)t\right]\left\langle \widehat{\mathbf{E}}_s^{\dagger}(\omega)\,\widehat{\mathbf{E}}_s(\omega')\right\rangle d\omega d\omega' \quad . \tag{10}$$

Let's define the scalar autocovariance of the source field as

$$G(\tau) = \left\langle \mathbf{E}_s^{\dagger}(t-\tau)\,\mathbf{E}_s(t)\right\rangle \quad , \tag{11}$$

with the property

$$G^*(\tau) = G(-\tau) \quad , \tag{12}$$

which ensures that the Fourier transform $\widehat{G}(\omega)$, denoted hereafter $S(\omega)$ for power spectrum, is real. For the expectation $\left\langle \mathbf{E}_s^{\dagger}(\omega)\,\mathbf{E}_s(\omega')\right\rangle$ we have

$$\begin{aligned}\left\langle \widehat{\mathbf{E}}_s^{\dagger}(\omega)\,\widehat{\mathbf{E}}_s(\omega')\right\rangle &= \int_{-\infty}^{\infty}\int_{-\infty}^{\infty}\exp\left[-i(\omega' t_2-\omega t_1)\right]\left\langle \mathbf{E}_s^{\dagger}(t_1)\,\mathbf{E}_s(t_2)\right\rangle dt_1 dt_2 \\ &= \int_{-\infty}^{\infty}\int_{-\infty}^{\infty}\exp\left[-i(\omega' t_2-\omega t_1)\right] G(t_2-t_1)\,dt_1 dt_2 \quad ,\end{aligned} \tag{13}$$

which may be reduced to

$$\left\langle \widehat{\mathbf{E}}_s^{\dagger}(\omega)\,\widehat{\mathbf{E}}_s(\omega')\right\rangle = \delta(\omega'-\omega)\int_{-\infty}^{\infty}\exp\left[-i\left(\frac{\omega'+\omega}{2}\right)s\right] G(s)\,ds = \delta(\omega'-\omega)\,S(\omega) \quad . \tag{14}$$

Inserting (14) into the expression for $\left\langle \mathbf{E}^{\dagger}(t)\,\mathbf{E}(t)\right\rangle$ gives us

$$\langle N(t)\rangle = \rho\left\langle \mathbf{E}^{\dagger}(t)\,\mathbf{E}(t)\right\rangle = \rho\int_{-\infty}^{\infty}|m(\omega,t)|^2\,S(\omega)\,d\omega \quad . \tag{15}$$

In the integrand we have

$$|m(\omega,t)|^2 = \alpha_1^2 + \left|\widehat{\beta}_2(\omega)\right|^2 + 2\alpha_1\,\mathrm{Re}\left\{\widehat{\beta}_2(\omega)\exp\left[-i\phi_1(\omega,t)+i\phi_2(\omega,t)\right]\right\} \quad . \tag{16}$$

The last term is the interference term, which is usually the focus of detection. After integrating we have

$$\langle I(t)\rangle = \frac{\rho e}{\Delta t}\int_{-\infty}^{\infty} r(t-t')\left[\int_{-\infty}^{\infty}|m(\omega,t')|^2\,S(\omega)\,d\omega\right]dt' \quad . \tag{17}$$

2.3. Autocovariance of the photocurrent

The autocovariance of the photocurrent is given by

$$\begin{aligned}K_I(t,t') &= \langle I(t)\,I(t')\rangle - \langle I(t)\rangle\,\langle I(t')\rangle \\ &= \left(\frac{e}{\Delta t}\right)^2\int_{-\infty}^{\infty}\int_{-\infty}^{\infty} r(t-t_1)\,r(t'-t_2)\,K_N(t_1,t_2)\,dt_1 dt_2 \quad ,\end{aligned} \tag{18}$$

where $K_N(t_1,t_2)$ is the autocovariance of the random process $N(t)$ given by

$$K_N(t_1,t_2) = \left[\langle N(t_1)\rangle\,\delta(t_1-t_2) + K_{\overline{N}}(t_1,t_2)\right] \quad . \tag{19}$$

The second term in the square brackets is given by

$$K_{\overline{N}}(t_1,t_2) = \left\langle \overline{N}(t_1)\,\overline{N}(t_2)\right\rangle - \left\langle \overline{N}(t_1)\right\rangle \left\langle \overline{N}(t_2)\right\rangle \quad . \tag{20}$$

We can find an expression for this covariance in terms of the statistical properties of the source

$$\begin{aligned}\left\langle \overline{N}(t_1)\,\overline{N}(t_2)\right\rangle &= \rho^2 \left\langle \mathbf{E}^\dagger(t_1)\,\mathbf{E}(t_1)\,\mathbf{E}^\dagger(t_2)\,\mathbf{E}(t_2)\right\rangle \\ &= \rho^2 \left\langle \overline{N}(t_1)\right\rangle \left\langle \overline{N}(t')\right\rangle + \rho^2 tr\left[\left\langle \mathbf{E}(t_1)\,\mathbf{E}^\dagger(t_2)\right\rangle \left\langle \mathbf{E}(t_2)\,\mathbf{E}^\dagger(t_1)\right\rangle\right] \quad .\end{aligned} \tag{21}$$

In this equation we used the assumption that the components of the electric field have circular Gaussian statistics, and that the overall statistics of the field are also Gaussian.[8] For the $K_{\overline{N}}(t,t')$ we now have

$$\begin{aligned}K_{\overline{N}}(t_1,t_2) &= \rho^2 tr\left[\left\langle \mathbf{E}(t_1)\,\mathbf{E}^\dagger(t_2)\right\rangle \left\langle \mathbf{E}(t_2)\,\mathbf{E}^\dagger(t_1)\right\rangle\right] \\ &= \rho^2 tr\left[\mathbf{J}(t_1,t_2)\,\mathbf{J}^\dagger(t_1,t_2)\right] \quad ,\end{aligned} \tag{22}$$

where

$$\mathbf{J}(t_1,t_2) = \left\langle \mathbf{E}(t_1)\,\mathbf{E}^\dagger(t_2)\right\rangle \quad . \tag{23}$$

The matrix autocovariance of the source is

$$\mathbf{G}(\tau) = \left\langle \mathbf{E}_s(t)\,\mathbf{E}_s^\dagger(t-\tau)\right\rangle \quad . \tag{25}$$

This definition assumes stationarity at the source. This matrix has the property

$$\mathbf{G}(-\tau) = \mathbf{G}^\dagger(\tau) \quad , \tag{26}$$

and is related to the scalar autocovariance via

$$G(\tau) = tr\left[\mathbf{G}(\tau)\right] \quad . \tag{27}$$

We can compute the matrix $\mathbf{J}(t_1,t_2)$ as

$$\mathbf{J}(t_1,t_2) = \int_{-\infty}^{\infty}\int_{-\infty}^{\infty} m(\omega,t_1)\,m^*(\omega',t_2)\exp\left[i(\omega t_1 - \omega' t_2)\right]\left\langle \widehat{\mathbf{E}}_s(\omega)\,\widehat{\mathbf{E}}_s^\dagger(\omega')\right\rangle d\omega d\omega' \quad , \tag{28}$$

where

$$\left\langle \widehat{\mathbf{E}}_s(\omega)\,\widehat{\mathbf{E}}_s^\dagger(\omega')\right\rangle = \delta(\omega'-\omega)\int_{-\infty}^{\infty}\exp\left[-i\left(\frac{\omega'+\omega}{2}\right)s\right]\mathbf{G}(s)\,ds = \delta(\omega'-\omega)\,\mathbf{G}(\omega) \quad . \tag{29}$$

Inserting the above expression into the expression for $\mathbf{J}(t,t')$ we get

$$\mathbf{J}(t,t') = \int_{-\infty}^{\infty} m(\omega,t)\,m^*(\omega,t')\exp\left[i\omega(t-t')\right]\mathbf{G}(\omega)\,d\omega \quad . \tag{30}$$

Moving to the trace step we have $K_{\overline{N}}(t,t')$ given by

$$\rho^2\int_{-\infty}^{\infty}\int_{-\infty}^{\infty} m(\omega,t_1)\,m^*(\omega,t_2)\,m^*(\omega',t_1)\,m(\omega',t_2)\exp\left[i(\omega-\omega')(t_1-t_2)\right]tr\left[\widehat{\mathbf{G}}(\omega)\,\widehat{\mathbf{G}}^\dagger(\omega')\right]d\omega d\omega' \quad . \tag{31}$$

Finally, the covariance of the current is given by

$$\begin{aligned}\left\langle I(t)\,I(t')\right\rangle - \left\langle I(t)\right\rangle\left\langle I(t')\right\rangle &= \left(\frac{e}{\Delta t}\right)^2\int_{-\infty}^{\infty} r(t-t_1)\,r(t'-t_1)\left\langle N(t_1)\right\rangle dt_1 \\ &\quad + \left(\frac{e}{\Delta t}\right)^2\int_{-\infty}^{\infty}\int_{-\infty}^{\infty} r(t-t_1)\,r(t'-t_2)\,K_{\overline{N}}(t_1,t_2)\,dt_1 dt_2 \quad .\end{aligned} \tag{32}$$

It can be shown that because the light field oscillates at about $10^{13}Hz$, the second term of (32) is negligible. We are thus in this case Poisson noise limited.

2.4. Computing detectability and associated AUC

The detectability associated with the Hotelling observer can be shown to be given by[9]

$$d^2 = \mathbf{X}^\dagger \mathbf{K}^{-1} \mathbf{X} = \mathbf{X}^\dagger \mathbf{W} \quad , \tag{33}$$

where $\mathbf{X}$ is the vector signal through time where each component is the difference in the mean photocurrent under the two hypotheses, $\mathbf{K}$ is the associated mean covariance matrix under both hypotheses, and $\mathbf{W}$ equal $\mathbf{K}^{-1}\mathbf{X}$. We thus have

$$X_n = \langle I_1(t_n) \rangle - \langle I_0(t_n) \rangle \quad , \tag{34}$$

and

$$K_{m,n} = \frac{1}{2} K_0(t_n, t_m) + \frac{1}{2} K_1(t_n, t_m) \, . \tag{35}$$

2.5. Sample Description

To model a resolution task, we first need to define a sample model to be imaged. In this investigation we shall define a simple two layers sample to yield insight into the problem. The reflection term $\widehat{\beta}_2(\omega)$ corresponding to two reflections from that sample is illustrated in Fig. 2. The first interface is the boundary between air and a medium of refractive index n. The second interface is the boundary between the medium of refractive index n and a medium of refractive index n + Δn. These two interfaces are assumed to be parallel to one another and are separated by a distance ℓ. The refractive indices are assumed to be constant as a function of frequency. The reflection from this sample is given in (36), with Fresnel reflections at each interface r_1 and r_2 , and a phase delay $\delta(\omega)$ given by (37), with c being the speed of light.

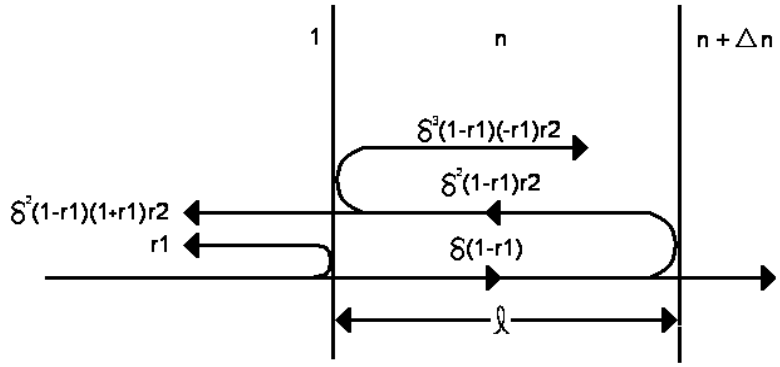

Figure 3. Illustration of the sample

$$\widehat{\beta}_2(\omega) = r_1 + (1 - r_1^2) r_2 \delta^2(\omega) \tag{36}$$

$$\begin{aligned} r_1 &= \frac{1-n}{1+n}, \\ r_2 &= \frac{-\Delta n}{2n + \Delta n} \\ \delta(\omega) &= \exp(i\omega \frac{n\ell}{c}) \quad . \end{aligned} \tag{37}$$

2.6. Task Description

In this study, we are concerned with a resolution task, for which an observer must determine whether two interfaces can be resolved. In the resolution task, the null hypothesis H_0 is taken to be both interfaces present with ℓ equal 0 , and the positive hypothesis H_1 is taken to be both interfaces present in the sample separated by some distance $\ell = \ell_0$. For H_1, ℓ_0 is increased from zero to see how the detectability index and the AUC vary.

3. RESULTS

3.1. Task Description

In order to properly simulate the detectability associated with the resolution task defined in 2.6, we must first choose reasonable input parameters for our theoretical setup. For the light source, defined by the power spectral density (PSD) $S(\omega)$, we chose the output of a superluminescent diode (SLD) with a power of 3mW. The PSD shown in Fig. 3 is sampled every 422.5GHz for a total of 160 samples.

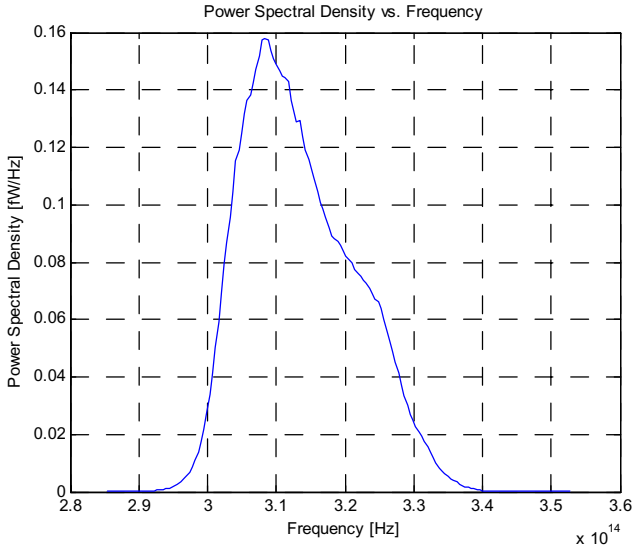

Figure 4. PSD of the light source

The constant α_1 defining the reflection from the reference mirror is taken as 1, and the phase terms $\phi_1(\omega, t)$ and $\phi_2(\omega, t)$ are set to $\omega\frac{2\ell_r}{c}$ and $\omega\frac{2\ell_s}{c}$, respectively. The constants ℓ_r and ℓ_s are the distances from the point where the field is split to the initial location of the reference mirror and the sample, respectively. For the purpose of the simulation, ℓ_s is chosen to be 3mm, and ℓ_r is chosen to be 3mm minus 14μm. Other important parameters in the simulation are chosen as follows: a refractive index n of 1.4 that represents skin, a detector responsivity of 1 for all frequencies, a detector area of 0.79mm^2 (resulting in a ρ of 1.3097x10$^{10}\frac{\mathrm{m}^2}{\mathrm{V}^2\mathrm{s}}$), a scan speed v_m of 0.09275m/s, a total scan distance of 74.2μm, a scan time of 0.8ms sampled every 0.4μs for a total of 2000 samples, and a detector integration time Δt of 4μs.

3.2. Computation of AUC for a fixed index of refaction change and a variable thickness layer

In a first simulation, we fixed the index of refraction change to $10^{-6}$and varied the thickness layer from 1 to 14μm. Results show as expected that the AUC increases with increased thickness. Also, within the coherence length of the source, oscillations are observed in the AUC which correspond to within layer interference. While such phenomena is not speckle because we are only dealing here with two layers, the interference between layers

is reminiscent of speckle and speckle will be caused within a more sofisticated tissue model by multiple scatterer interferences within the coherence length of the source. Interestingly, even beyond the layer thickness of $10\mu m$ which exceeds the coherence length of the source, the AUC value asymptotes at 0.8 instead of 1. Therefore, such layer will be resolved only with a 80% probability at most regardless of ℓ_0. Such result points to the importance of assessing resolution as a function of the biological sample to be imaged, not solely as a function of the light source.

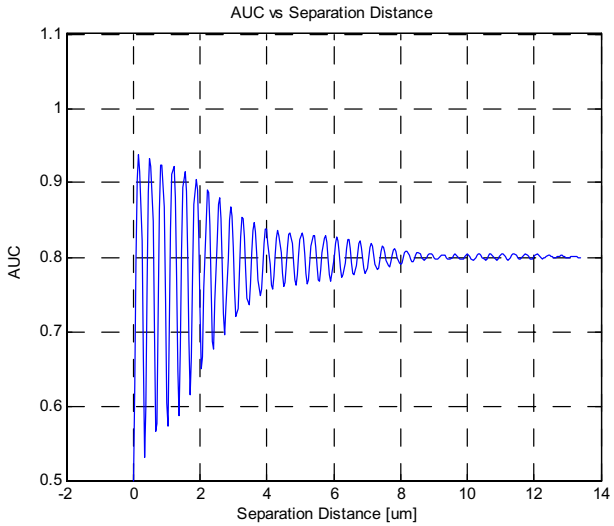

Figure 5. AUC versus ℓ for a Δn equal 10^{-6}

For biological cells, the refractive index of extracellular fluid ranges from 1.348-1.352, the refractive index of a cell membrane and protein aggregates range from 1.350-1.460,[10–11] the refractive index of cytoplasm ranges from 1.358-1.374,[10,13] and the refractive index of the cell nucleus ranges from 1.387-1.397.[10,14] If we assume these ranges to represent distributions of the refractive indices, we can compute the probable changes in refractive index across interfaces. The results of this calculation and some other information are shown in Table 1.[10,15] Changes in index of refractions are found to be in the order 10^{-2} for various structures.

Table 1. Cellular Refractive Indices and Variances

	Extracellar Fluid	Cell Membrane	Cytoplasm	Cell Nucleus
Range	1.348-1.352	1.350-1.460	1.358-1.374	1.387-1.397
Mean	1.350	1.405	1.366	1.392
Variance	0.002	0.055	0.008	0.005
Δn	0.005±0.0550		NA	NA
Δn	NA	0.039±0.0556		NA
Δn	NA	NA	0.026±0.0094	

We thus investigated many other cases, and two of these cases for Δn equal $10^{-5}$and 10^{-2} are shown in Fig. 6(a-b). Results show that for stronger layers as defined by Δn, the AUC asymtotes to 1 within the coherence length of the source. Specifically for Δn equal 10^{-2}, the AUC is 1 regardless of ℓ_0.Such findings point to the fact that detectability is predicted to be high even for structures sizes within the resolution of the OCT imaging system. Such theoretical findings is consistent with previous observations for e.g. by Richards-Kortum and associates, who state that "changes in scattering occur on a microscopic spatial scale well below the typical resolution of OCT imaging systems, yet these changes still impact OCT images".[4]

4. CONCLUSION

The mathematical framework presented is this paper allows the investigation of resolution in OCT, not solely based on the source power spectrum but also on the system noise and the tissue sample under measurement. Future investigations will include more sophisticated models of the tissue sample, as well as the effect of various hardware parameters. We shall also extend the investigation to other medical tasks such as detection and estimation. The goal of such investigation is hardware optimization.

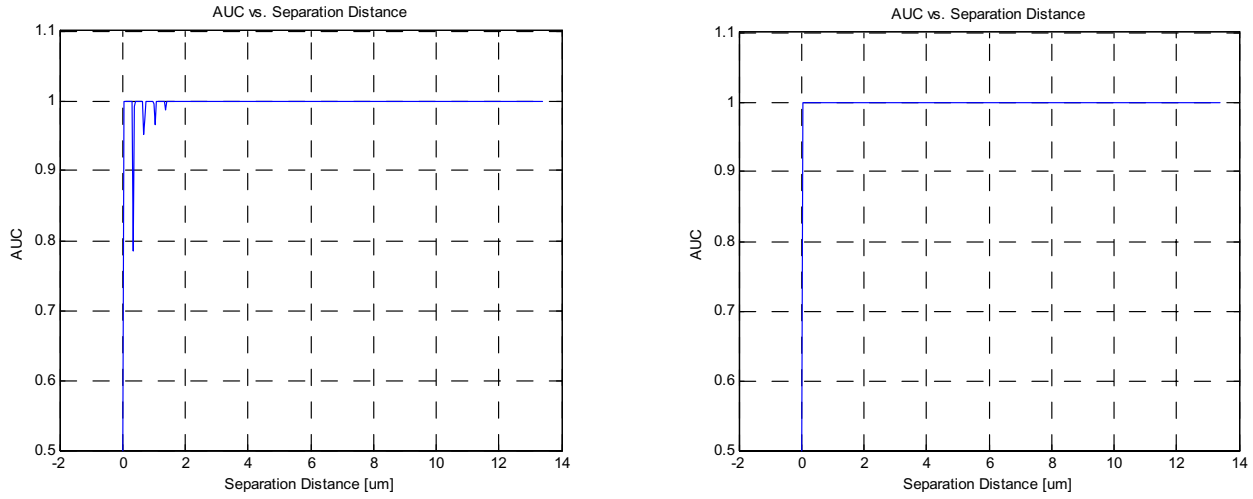

a b

Figure 6. Plot of AUC as a function of ℓ_0 for Δn equal 10^{-5} (a) and 10^{-2} (b),respectively.

5. ACKNOWEDLGEMENTS

We thank Harry Barrett and Kyle Myers for stimulating discussion about this work. This work was supported in part from the NIH/NCI CA87017, the NSF/IIS 00-82016 ITR, the US Army STRICOM, the UCF Presidential Instrumentation Initiative, and the DARPA & NSF PTAP program.

6. REFERENCES

1. D. Huang, E.A. Swanson, C. P. Lin, J. S. Schuman, W.G. Stinson, W. Chang, M. R. Hee, T. Flotte, K. Gregory, C. A. Puliafito, J. G. Fujimoto, "Optical coherence tomography," Science 254(5035), 1178-1181 (1991).

2. A. F. Fercher, W. Drexler, C. K. Hitzenberger, and T. Lasser, "Optical coherence tomography-principles and applications," Rep. Prog. Phys. 66 239-303 (2003).

3. J. M. Schmitt, "Optical Coherence Tomography(OCT): A Review," IEEE J. Select. Topics Quantum Electron. 5, No.4, 1205 (1999).

4. B. E. Bouma, and G. J. Tearney eds., Handbook of Optical Coherence Tomography, (Marcel Dekker, Inc., New York, (2002).

5. A. Dubois, L.Vabre, A.C. Boccara, E. Beaurepaire "High resolution full-field optical coherence tomography with a Linnik microscope", Applied Optics 41(4), 805-812, (2002).

6. C. Akcay, P. Parrein, and J. P. Rolland, "Estimation of longitudinal resolution in optical coherence imaging," Appl. Opt. 41(25), 5256-5262 (2002).

7. A.C.Akcay, J.P. Rolland, and J.M. Eichenholz, "Spectral shaping to improve the point spread function in optical coherence tomography," Optics Letters 28(20), 1921-1923 (2003).

8. H. H. Barrett, and K. J. Myers, Foundations of Image Science, Willey Series in Pure and Applied Optics, Ed. B.E.A. Saleh. (2004).

9. H. Hotelling, "The generalization of Student's ratio," Ann. Math. Stat. 2, 360 (1931).

10. A. Dunn, "Light Scattering Properties of Cells",
http://www.nmr.mgh.harvard.edu/~adunn/papers/dissertation/.

11. J. S. Maier, S. A. Walker, et al., "Possible correlation between blood glucose conentration and the reduced scattering coefficent of tissue in the near infrared", *Optics Letters*, 19, 2062-2064 (1994).

12. F. Lanni, A. Waggoner, and D. Taylor, "Internal reflection fluorescence microscopy", *Journal of Cell Biology*, 100, 1091, (1985).

13. A. Brunsting and P. Mullaney, "Differential light scattering from spherical mammalian cells", *Biophysical Journal*, 14, 439-453, (1974).

14. G. Elert and J. Shloming, "Thickness of a cell membrane",
http://hypertextbook.com/facts/2001/JenniferShloming.shtml.